Synthesis of Square Bi_2WO_6 Nanoplates as High-Activity Visible-Light-Driven Photocatalysts

Chuan Zhang† and Yongfa Zhu*

Department of Chemistry, Tsinghua University, Beijing, 100084, People's Republic of China

Received January 21, 2005. Revised Manuscript Received April 29, 2005

Square Bi_2WO_6 nanoplates have been successfully synthesized by simple hydrothermal process. The effects of hydrothermal temperature and reaction time on morphologies and sizes of the nanoplates were investigated. These nanoplates are square geometric shapes having their basal plane as the (001) plane of orthorhombic Bi_2WO_6. On the basis of results of morphologies observation and selected area electron diffraction of series samples, a possible growth mechanism of the nanoplates is revealed. The square laminar shape could be attributed to anisotropic growth along the (001) plane, which is parallel to their intrinsic layer structure. UV−visible diffuse reflection spectra of the prepared Bi_2WO_6 nanoplates indicate they had absorption in the visible region, but a blue shift appeared compared to their bulk counterparts. Their photocatalytic activities are determined by rhodamine B degradation under visible light irradiation ($\lambda > 400$ nm). The reaction constant (k) of the best quality Bi_2WO_6 nanoplates is three times that of the sample prepared by solid-state reaction, which indicates much higher photocatalytic activities of the nanoplates performed under visible light irradiation.

1. Introduction

Great interests in nanostructured materials have been focused on controlling the shapes of materials and finding novel properties.[1] Due to their unique properties and promising applications in electrical, optical, and magnetic devices, many materials have been shaped into different morphology nanostructures, such as nanotubes, nanowires, and nanobelts, etc.[2−5]

A two-dimensional nanostructure such as nanoplates is an important category of nanostructured materials to which increasing attention has been paid recently.[6,7] These nanoplate materials are usually characterized by high crystallinity and well-defined chemical composition as well as extremely high anisotropy with an ultrathin thickness. They are superior over spherical nanocrystallines as building blocks for constructing nanodevices and other applications with crystal orientation controlled by a "bottom-up" method due to their anisotropic structures. But up to now, 2D nanoplate synthesis is only explored in a narrow system, including some metals, such as Ag,[6,8] Au,[7,9] Cu,[10] Co,[11] Bi,[12] Pd, and Ni;[13] some simple metal oxides, metal sulfides, such as MgO,[14] Gd_2O_3,[15] SnO_2,[16] Cu_2S,[17] and CdS;[18] and other simple compounds such as $NbSe_2$[19] and LaF_3.[20] Still unknown are the following questions: Can other multicomponent oxides with unique properties be shaped to nanoplates, and how can that be achieved? Unlike the synthesis of monodispersed spherical particles, as well as the one-dimension nanorods/nanowires, which has been successful in many cases, systematic control of the size of nanoplates, i.e., the control of crystal growth in two dimensions, has been shown to be much more difficult. Traditional shape controlled synthesis methods could be clarified as two strategies: one is based on physical technologies, including thermal evaporation,[21] physical exfoliation,[22] and so on; the other is soft chemical methods, including hydrothermal or solvothermal synthesis,[1,23] surfactant

* To whom correspondence should be addressed. Telephone: +86-10-62783586. Fax: +86-10-62787601. E-mail: zhuyf@mail.tsinghua.edu.cn.
† E-mail: zhangchuan99@mails.tsinghua.edu.cn.

(1) Burda, C.; Chen, X.; Narayanan, R.; El-Sayed, M. A. *Chem. Rev.* **2005**, *105*, 1025.
(2) Iijima, S.; Ichihashi, T. *Nature* **1993**, *36*, 603.
(3) Pan Z. W.; Dai Z. R.; Wang Z. L. *Science* **2001**, *291*, 1947.
(4) Morales, A. M.; Lieber, C. M. *Science* **1998**, *279*, 208.
(5) Wu, Y.; Yang, P. *Chem. Mater.* **2000**, *12*, 605.
(6) Chen, S.; Fan, Z.; Carroll, D. L. *J. Phys. Chem. B.* **2002**, *106*, 10777.
(7) Hu, J.; Zhang, Y.; Liu, B.; Liu, J.; Zhou, H.; Xu, Y.; Jiang, Y.; Yang, Z.; Tian, Z.-Q. *J. Am. Chem. Soc.* **2004**, *126*, 9470.
(8) (a) Sun, Y.; Mayers, B.; Xia, Y. *Nano Lett.* **2003**, *3*, 675. (b) Aslan, K.; Lakowicz, J. R.; Geddes, C. D. *J. Phys. Chem. B* **2005**, *109*, 6247. (c) Sun, Y.; Xia, Y. *Adv. Mater.* **2003**, *15*, 695.
(9) (a) Kirkland, A. I.; Jefferson, D. A.; Duff, D. G.; Edwards, P. P.; Gameson, I.; Johnson, B. F. G.; Smith, D. *J. Proc. R. Soc. London, A* **1993**, *440*, 589. (b) Tsuji M.; Hashimoto M.; Nishizawa Y.; Tsuji T. *Chem. Lett.* **2003**, *32*, 1114. (c) Shao Y.; Jin Y. D.; Dong S. J. *Chem. Commun.* **2004**, *9*, 1104. (d) Zhou, Y.; Wang, C. Y.; Zhu, Y. R.; Chen, Z. Y. *Chem. Mater.* **1999**, *11*, 2310.
(10) Curtis, A. C.; Duff, D. G.; Edwards, P. P.; Jefferson, D. A.; Johnson, B. F. G.; Kirkland, A. I.; Wallace, A. S. *Angew. Chem., Int. Ed. Engl.* **1988**, *27*, 1530.
(11) (a) Puntes, V. F.; Krishnan, K. M.; Alivisatos, A. P. *Science* **2001**, *291*, 2115. (b) Puntes, V. F.; Zanchet, D.; Erdonmez, C. K.; Alivisatos, A. P. *J. Am. Chem. Soc.* **2002**, *124*, 12874.
(12) Bradley, J. S.; Tesche, B.; Busser, W.; Maase, M.; Reetz, M. T. *J. Am. Chem. Soc.* **2000**, *122*, 4631.
(13) Fu, R.; Xu, S.; Lu, Y.-N.; Zhu, J.-J. *Cryst. Growth Des.*, in press.
(14) Yu, J. C.; Xu, A.; Zhang, L.; Song, R.; Wu, L. *J. Phys. Chem. B* **2004**, *108*, 64.
(15) Cao, Y. C. *J. Am. Chem. Soc.* **2004**, *126*, 7456.
(16) Ohgi, H.; Maeda, T.; Hosono, E.; Fujihara, S.; Imai, H. *Cryst. Growth Des.* **2005**, *5* (3), 1079.
(17) Zhang, H. T.; Wu, G.; Chen, X. H. *Langmuir* **2005**, *21*, 4281.
(18) Pinna, N.; Weiss, K.; Urban, J.; Pileni, M. P. *Adv. Mater.* **2001**, *13*, 261.
(19) Sekar, P.; Greyson, E. C.; Barton, J. E.; Odom, T. W. *J. Am. Chem. Soc.* **2005**, *127*, 2054.
(20) Zhang, Y. W.; Sun, X.; Si, R.; You, L. P.; Yan, C. H. *J. Am. Chem. Soc.* **2005**, *127*, 3260.
(21) Liang, C. H.; Shimizu, Y.; Sasaki, T.; Umehara, H.; Koshizaki, N. *J. Phys. Chem. B* **2004**, *108*, 9728.

10.1021/cm0501517 CCC: $30.25
Published on Web 06/01/2005

assistant,[1,6,24] and molecular assemblies as soft templates, etc.[8a,18] Among later ones, hydrothermal synthesis always can be carried out by a simple process and has been demonstrated as a versatile pathway toward such shape controlled nanocrystals, using either multiple-source precursors or single-source precursor. Until now, several growth mechanisms about the morphologies formation have successfully explained 1D nanocrystal growth in the hydrothermal process.[1,25] For 2D nanostructure, however, it is not very clear how the nanoplates formed and why different morphologies of nanoplates appeared. For instance, Ag nanoplates may appear as triangle or hexagon shapes in different conditions.[8] Although various morphologies may appear, there is no doubt that nanoplate formation and shape appearances are strongly related to their instinct atomic structure. It is indispensable to reveal this relationship for better shape control in 2D nanoplate synthesis.

Generally, crystal growth under hydrothermal condition is a typical bottom-up process, which plays an important role in the fabrication of nanostructured materials due to its potential in simultaneously controlling the size, morphology, and dispersivity of nanocrystals.[26] From the viewpoint of bottom to top, layer structured materials could be regarded as plenty of layer stacks.[27] If we could control the crystalline growth along the layer, nanoplates can be prepared. The Aurivillius family of structurally related oxides with general formula $Bi_2A_{n-1}B_nO_{3n+3}$ (A = Ca, Sr, Ba, Pb, Bi, Na, K and B = Ti, Nb, Ta, Mo, W, Fe) usually had the layer structure and unique properties.[28] Bi_2WO_6 was the simplest member when $n = 1$ was originally of interest because of the excellent intrinsic physical and chemical properties. It has been found to possess interesting physical properties such as ferroelectric piezoelectricity, pryoelectricity, catalytic behavior, oxide anion conducting, and a nonlinear dielectric susceptibility.[29] Recently, Kudo and Hijii found the Bi_2WO_6 had photocatalytic activities for O_2 evolution and Zou et al. revealed the Bi_2WO_6 could degrade the organic compound under visible light irradiation.[30,31] Their works revealed Bi_2WO_6 could perform as excellent photocatalytic materials and solar energy transfer materials. However, all Bi_2WO_6 samples were prepared by solid-state reaction in their work, and the photocatalytic activities were not high. Nanostructured photocatalysts usually had high photocatalytic activities because of their special morphologies, high surface areas, and high efficiency of electron−hole separation according to lots of previous research on TiO_2.[32−35] So Bi_2WO_6 nanoplate fabrication has special significance in promoting its photocatalytic performance and other unique properties. In this work, it demonstrated the photocatalytic activities significantly promoted when the Bi_2WO_6 was shaped to nanoplates. We also found formation of the nanoplates is strongly related to their layer structure. As the simplest member of the Aurivillius family, the mechanism of Bi_2WO_6 nanoplates formation could afford guidance for the other Aurivillius family nanoplate fabrications.

2. Experimental Section

2.1. Synthesis of the Samples. Bi_2WO_6 nanoplates were synthesized through hydrothermal process. All chemicals used were analytic grade reagents without further purification. The start materials were corresponding Na_2WO_4 and $Bi(NO_3)_3$ in 1:2 molar ratio. The start materials (5 mmol Bi) were mixed together, and 100 mL of deionized water was added. White precipitates appeared immediately, and the beaker was putted in ultrasonic bath for 10 minutes in order to complete the precipitate reaction. Washing for several times, the collected precipitate was added into a 50 mL Teflon-lined autoclave and filled with deionized water up to 80% of the total volume. After that, the autoclave was sealed into a stainless steel tank and kept at series experiment condition. All temperature series samples were treated from 100 to 240 °C for 12 h, while all time series samples were prepared at 160 °C for different hours. Then the reactor was cooled to room-temperature naturally. Resulting samples were collected and washed with deionized water and dried at 80 °C in air. Meanwhile Bi_2WO_6 were synthesized by traditional solid-state reaction according to ref 31 for comparisnon with the nanoplates.

2.2. Charaterization. Purity and crystallinity of the as-prepared sample was characterized by powder X-ray diffraction (XRD) on Bruker D8-advance X-ray diffractometer at 40 kV and 40 mA for monochromatizaed Cu Kα (λ = 1·5418 Å) radiation. Diffraction patterns from powdered samples held on quartz zero background plates were obtained by $\theta-\theta$ geometry. The XRD data for indexing and cell-parameter calculation were collected in a scan mode with a step length of 0.02° and a preset time of 0.4 s/step. Morphologies and structures of the prepared samples were further examined with transmission electron microscopy (TEM) by a JEM 1010 electron microscope operated at an accelerating voltage of 120 kV. High-resolution transmission electron microscopy (HRTEM) images were

(22) (a)Wang, L. Z.; Omomo, Y.; Sakai, N.; Fukuda, K.; Nakai, I.; Ebina, Y.; Takada, K.; Watanabe, M.; Sasaki, T. *Chem. Mater.* **2003**, *15*, 2873. (b) Omomo, Y.; Sasaki, T.; Wang, L. Z.; Watanabe, M. *J. Am. Chem. Soc.* **2003**, *125*, 3568. (c) Gautam, U. K.; Vivekchand, S. R. C.; Govindaraj, A.; Kulkarni, G. U.; Selvi, N. R.; Rao, C. N. R. *J. Am. Chem. Soc.* **2005**, *127*, 3658.
(23) (a) Dias, A.; Ciminelli, V. S. T. *Chem. Mater.* **2003**, *15*, 1344. (b) Livage, C.; Egger, C.; Ferey, G. *Chem. Mater.* **2001**, *13*, 410.
(24) Liu, Z.; Yang, Y.; Liang, J.; Hu, Z.; Li, S.; Peng, S.; Qian, Y. *J. Phys. Chem. B* **2003**, *107*, 12658
(25) Cushing, B. L.; Kolesnichenko, V. L.; O'Connor, C. *J. Chem. Rev.* **2004**, *104*, 3893.
(26) Xia, Y.; Yang, P.; Sun, Y.; Wu, Y.; Mayers, B.; Gates, B.; Yin, Y.; Kim, F.; Yan, H. *Adv. Mater.* **2003**, *15*, 353.
(27) (a) Sivakumar, T.; Seshadri, R.; Gopalakrishnan, J. *J. Am. Chem. Soc.* **2001**, *123*, 11496. (b) Nagata H, Takahashi T, Chikushi N, Takenaka T. *Ferroelectrics* **2000**, *241*, 1953. (c) Karen, P.; Woodward, P. M. *J. Mater. Chem.* **1999**, *9*, 789.
(28) (a) Kendall, K. R.; Navas, C.; Thomas, J. K.; zur Loye, H. C.; *Chem. Mater.* **1996**, *8*, 642. (b) Tsunoda, Y.; Shirata, M.; Sugimoto, W.; Liu, Z.; Terasaki, O.; Kuroda, K.; Sugahara, Y. *Inorg. Chem.* **2001**, *40*, 5768. (c) Kim, J. Y.; Chung, I.; Choy, J. H.; Park, G. S. *Chem. Mater.* **2001**, *13*, 2759. (d) Tsunoda, Y.; Sugimoto, W.; Sugahara, Y. *Chem. Mater.* **2003**, *15*, 632.
(29) (a) Newkirk, H. W.; Quadfing, P.; Liebertz, J.; Kockel, A. *Ferroelectrics* **1972**, *4*, 51. (b) Stefanovich, S. Yu.; Nenetsev, Yu. N. *Phys. Status Solidi A* **1973**, *20*, 49. (c) Ismailzade, I. G.; Mirishli, F. A. *Kristallografiya* **1970**, *14*, 738. (d) Yanovskii, V. K.; Voronkova, V. I.; Alexandrovskii, A. L.; D'yakov, V. A. *Dokl. Akad. Nauk SSSR* **1975**, *222*, 94. (e) Utkin, V. I.; Roginsksya, Yu. E.; Voronkova V. I.; Yanovskii, V. K.; Galyamov, B. Sh.; Venetsev, Yu. N. *Phys. Status Solidi A* **1980**, *59*, 75. (f) Herwood, P. *Ind. Chem.* **1963**, *39*, 242.
(30) Kudo, A.; Hijii, S. *Chem. Lett.* **1999**, 1103.
(31) Tang, J. W.; Zou, Z. G.; Ye, J. H. *Catal. Lett.* **2004**, *92*, 53.
(32) Stathatos E.; Petrova T,; Lianos P. *Langmuir* **2001**, *17*, 5025.
(33) Chu S. Z.; Inoue S.; Wada K.; Li D.; Haneda H. *J. Mater. Chem.* **2003**, *13*, 866.
(34) Chu S. Z.; Inoue S.; Wada K.; Li D.; Haneda H.; Awatsu S. *J. Phys. Chem. B* **2003**, *107*, 6586.
(35) Addamo, M.; Augugliaro, V.; Di Paola, A.; Garcia-Lopez, E.; Loddo, V.; Marci, G.; Molinari, R.; Palmisano, L.; Schiavello, M. *J. Phys. Chem. B* **2004**, *108*, 3303.

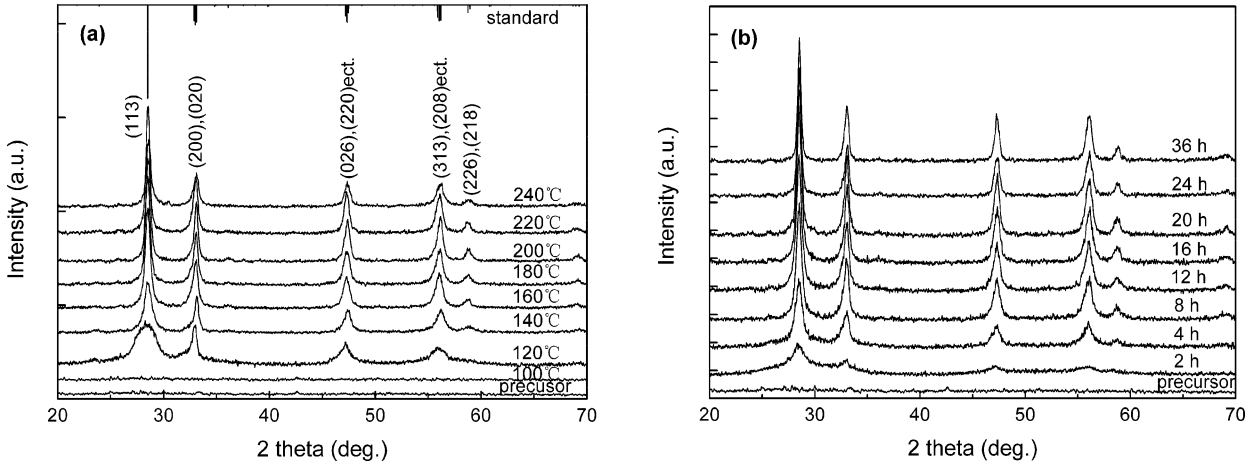

Figure 1. XRD pattern of series prepared Bi_2WO_6 crystallines (a) temperature series samples treated for 12 h and (b) time series samples treated at 160 °C.

obtained by JEM 2010F field emission gun transmission electron microscope operated at an accelerating voltage of 200 kV. Samples used for TEM characterization were dispersed in absolute ethanol and were ultrasonicated before observation, and then a drop of the diluted colloidal suspension of the sample was placed onto a Cu grid. After being air-dried, the specimen was subjected to TEM observations. UV−vis diffuse reflectance spectrums (DRS) of the samples were measured by using an Hitachi U-3010 UV−vis spectrophotometer. BET surface area was measured by ASAP 2010 V5.02H. The absorbed gas was nitrogen.

2.3. Photocatalytic Test. Photocatalytic activities of the Bi_2WO_6 nanoplates were evaluated by degradation of rhodamine-B under visible light irradiation of a 500 W Xe lamp with the 400 nm cutoff filter. The reaction cell was placed in a sealed black box of which the top was opened and the cutoff filter was placed to provide visible light irradiation. In each experiment, 0.1 g of photocatalysts without cocatalyst was added into 200 mL rhodamine-B solution (10^{-5} mol/L). After dispersing in ultrasonic bath for 5 min, the solution was stirred and espoused to visible light irradiation. The concentrations of the rhodamine-B were carried out using Hitachi U-3010 UV−vis spectrophotometer each 15 min.

3. Results and Discussion

3.1. Formation of the Bi_2WO_6 Crystalline. The starting precipitates and overall structure of the synthesized samples were characterized by XRD. Parts a and b of Figure 1 show the XRD pattern of temperature series samples and time series samples, respectively. In both Figure 1a,b, the starting precipitate precursors obtained by inorganic precipitate reaction were amorphous compound before hydrothermal treatment. In the temperature series condition demonstrated in Figure 1a, the crystalline formation needed the appropriate temperature. Crystal diffraction peaks were found when the temperature was no less than 120 °C. In the time series condition when the temperature was settled at 160 °C, the crystalline phase appeared only after 2 h hydrothermal treatment, which is shown in Figure 1b. All peaks of the XRD patterns shown in Figure 1a,b could be indexed according to Bi_2WO_6. After refinement, the cell constants of Bi_2WO_6 were calculated to be $a = 5.456$ Å, $b = 5.436$ Å, and $c = 16.426$ Å, which were consistent with the literature data and (JCPDS 73-1126). In both Figure 1a,b, expanded diffraction peaks obviously revealed the crystalline phase would be nanosized. Temperature effects on the crystalline phase were demonstrated through the changes of the XRD patterns in Figure 1a. At the temperature extent from 120−200 °C, the shape of diffraction peaks became more clean-cut and the intensities increased gradually, indicating better nanocrystallines formed. The crystallines grew larger as estimated according to the peak expansion on the basis of the famous Scherrer equation in that temperature range. However this situation reversed after 200 °C. The intensity of the diffraction peak decreased a little at 220 °C. For 240 °C, the XRD pattern was obviously different from the previous samples. On the other hand, reaction time effects on crystalline phase appeared to be similar to the situation with temperature series samples. The best XRD pattern was obtained for 20 h hydrothermal treatment. The longer or shorter reaction time led to low diffraction intensities or worse XRD patterns, indicating the crystallines were not as good as the 20 h sample. But it should be noticed that the reaction time effect was slighter compared to the temperature effect. For instance, the XRD pattern of the 36 h sample was nearly the same as that of the 20 h one, only except for a little intensity decreasing. At the top of Figure 1a, a standard XRD pattern of Bi_2WO_6 is given. The standard intensity of the (113) peak is about 5 times that of the (200) or (020) peak, which could be expressed as $I_{(113)}/I_{(200)} = 5$. However in the temperature series samples the value of $I_{(113)}/I_{(200)}$ was almost smaller than 2 below 200 °C. It implied the crystal had special anisotropic growth along the (001) plane. These results could be attributed to their square plates morphologies observed by TEM. When the temperature further increased, the value of $I_{(113)}/I_{(200)}$ grew. At 240 °C, the $I_{(113)}/I_{(200)}$ value was close to the standard. In the time series samples, this value is kept the same at about 2 before 20 h treatment, and after that the value increased but not evidently. All these changes implied the anisotropic morphologies of prepared samples had changed more or less.

3.2. Morphologies of the Bi_2WO_6 Samples. *Temperature Effects.* Morphologies of the Bi_2WO_6 synthesized by hydrothermal process were charactered by TEM. Figure 2a is the morphology of the starting precursor. It indicated that the starting precipitates were nanoparticles with irregular shape. Parts b−h of Figure 2 showed the morphologies of temperature series samples which were prepared in various tem-

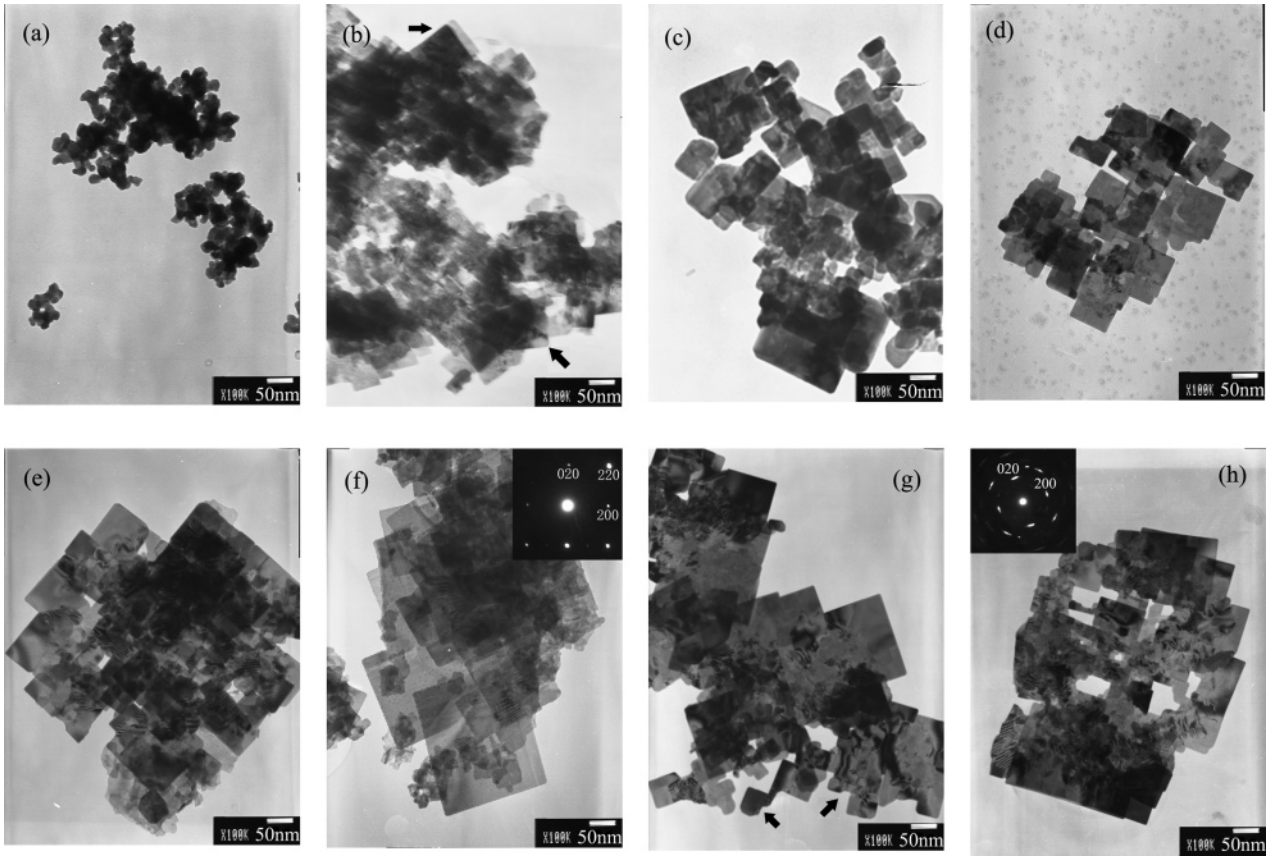

Figure 2. Morphologies of temperature series Bi_2WO_6 samples: (a) precursor; (b) 120 °C; (c) 140 °C; (d) 160 °C; (e) 180 °C; (f) 200 °C; (g) 220 °C; (h) 240 °C.

perature hydrothermal conditions. On the basis of TEM images, it could be found that the higher temperature treatment produced better nanoplates before 200 °C. At 120 °C, morphologies of the samples are distinguished from the precursor with a shaggy appearance, but some laminar structure could be found among irregular particles (see the arrows in Figure 2b). The irregular particles decreased, and Bi_2WO_6 crystalline exhibited an explicit edge, but the shape was still not regular for 140 °C. When the temperature was further increased to 160 °C, the samples usually had square-plate-like morphologies with a short edge. While the temperature achieved 200 °C, the square nanoplates grew larger and thinner. The length of the edge could reach 200 nm. As shown in the corner of Figure 2f, selective area electron diffraction (SAED) pattern of individual flat-lying nanoplates showed regular square diffraction spot array, corresponding to the lattice spacing of 0.273, 0.272 nm are from the (200), (020) Bragg reflection of the orthorhombic Bi_2WO_6, respectively. When temperature further increased to 220 °C, these nanoplates showed truncated corners or some breakage of the edges, making them have irregular outlines (see the arrows in Figure 2g). The plate-like morphology could still be observed but the square-plate seriously destroyed for 240 °C hydrothermal treatment. Some irregular holes appeared in the plate. At this moment, the pattern in the corner of Figure 2h showed a transitional status from single crystalline spot array to polycrystalline rings, indicating the destruction of the single-crystal feature.

Reaction Time Effects. The whole process of the nanoplate growth in details was obtained by morphology observation of time series samples, which is shown in Figure 3a−h. After 2 h treatment, the morphology was irregular similar to the precursor but not shaggy as before. Many tiny crystalline nuclei were formed at this time, which was confirmed by XRD results. At this point, SAED experiment, which is shown in the corner of Figure 3a, also confirmed that many polycrystalline particles existed. Some small square laminar structure appeared at 4 h hydrothermal treatment but mainly still irregular particles. For 8 h, more than half of the samples showed square laminar structure with a short edge in length. Small nanoplates formed and further grew with the cost of the small irregular nanoparticles. Finally the irregular nanoparticles almost disappeared when treatment time further increased to 12 h. After that, the small nanoplates grew much bigger and had a clear square laminar shape. For 20 h treatment, good-quality nanoplates could be obtained. At the corner of Figure 3f, the SAED pattern was the same as temperature samples'. The indexed select electron diffraction pattern for the (001) zone revealed the single-crystal nature of the nanoplates and confirmed that the nanoplates grow preferentially along the (001) plane, which were parallel to its instinct $a \times b$ layer plane. Over long time treatment led to diminution of the nanoplates and reduced its quality, which is shown in Figure 3h for the 36 h sample.

Growth Orientation. HRTEM observation was conducted to clarify the particular orientation of the nanoplates. Full view of the prepared nanoplates (200 °C, 12 h) was shown in Figure 4a. The rectangle part was enlarged 5 times, which is shown in Figure 4b. The edge of the nanolplates was explicit at the beginning but not stable under 200 KV electron

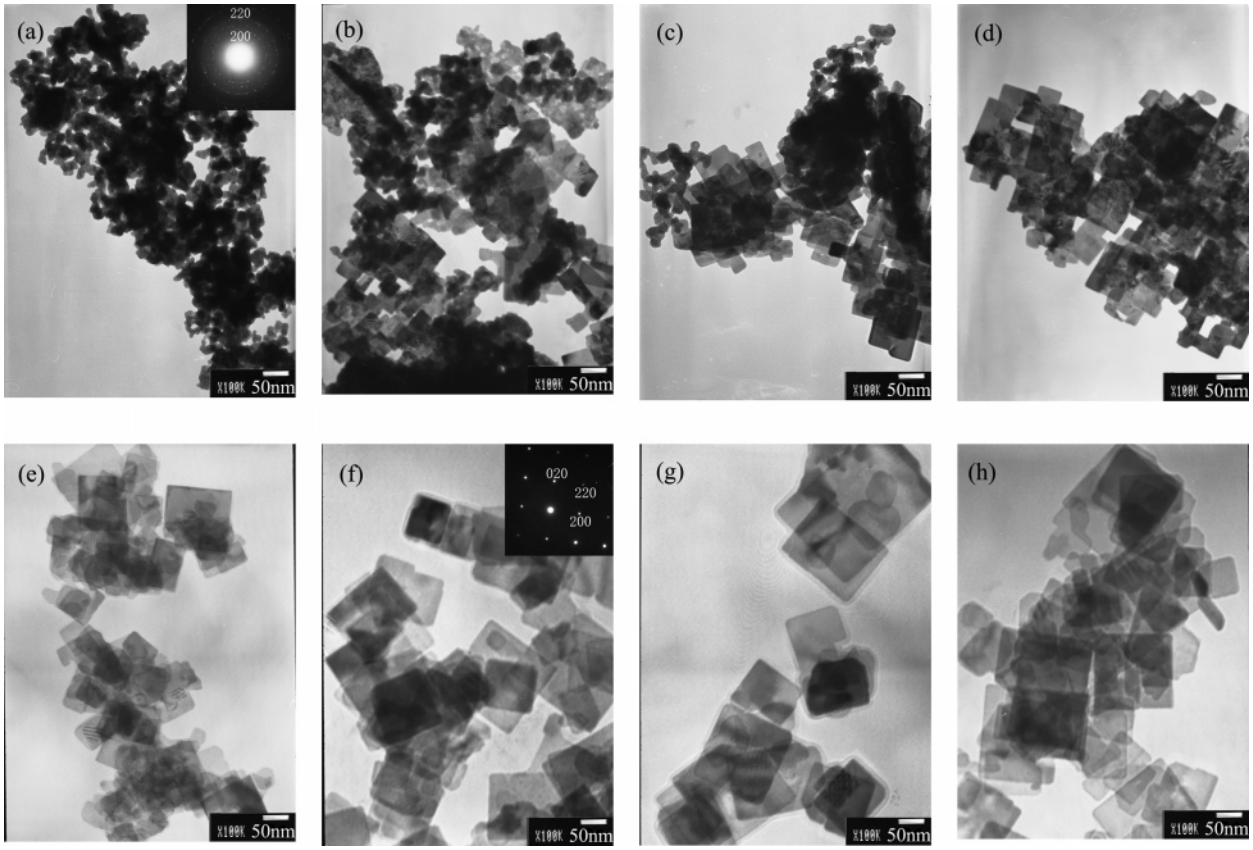

Figure 3. Morphologies of time series samples treated at 160 °C: (a) 2, (b) 4, (c) 8, (d) 12, (e) 16, (f) 20, (g) 24, and (h) 36 h.

exposure. The electron beam may create some crater on the basal plane and lead to further stochastic growth on the edge. SAED analysis was the same as that previously discussed. HRTEM images were shown in Figure 4c,d, which were the corner and crater areas of the nanoplate corresponding to rectangle A and rectangle B sections in Figure 4b. The growth orientation was the same in different areas, also indicating a single-crystalline feature of the whole nanoplates. Combining the HRTEM image and the SAED pattern, it can be measured that the *d* spacings are 0.273 and 0.272 nm, which agree well with the lattice spacings of (200) and (020) of orthorhombic Bi_2WO_6. These results also revealed the basal plane is a (001) plane, featuring a square arrangement of atoms along with the instinct layer. Energy dispersive analysis of X-rays (EDAX) was conducted for element constituents of the nanoplate, which are shown in Figure 4e. Only W and Bi were found in the spectrum except for the Cu brought by the Cu grid. Quantitative results give the atomic ratio of 6:3.2 for Bi/W. It was close to the ideal value of 2 considering the instrumental error.

Size and Thickness of the Nanoplates. To some extent, higher temperature or longer reaction time promotes the final size of the nanoplates. The lengths of the edges are listed in Table 1 and Table 2. However, excessively high temperature bought breakage of the nanoplates. In the time series sample, the length of the edge increased before 20 h and stayed about the same for 24 h but over the long reaction time led diminution of the crystalline and yields a worse quality of Bi_2WO_6 nanoplates for 36 h. The thickness of the nanoplates was difficult to clearly determine because the nanoplates were usually ultrathin and flat-lying on the Cu grid. Compared to the morphologies of different series sample, it could be noticed that temperature has much more effect on the thickness than reaction time. There was nearly no change between time series samples. In temperature series samples, the thickest was obtained at 140 °C. It was about 10 nm estimated by the gibbous edge. The thinnest one was obtained at 200 °C, and the thickness was about 5 nm estimated through the enlarged edge in Figure 4b, corresponding to three repeating units, i.e., 3×1.6 nm $= 4.8$ nm. Other samples usually have thickness between them. So the thickness of the nanoplates was in extent of 5−10 nm, which corresponds to 3−6 repeating units in the *c* axis.

3.3. Mechanism of the Nanoplate Formation. The Bi_2WO_6 formation was a typical hydrothermal ripening process:[36] a highly supersaturated solution was adopted, and amorphous fine particles acted as the precursor for the synthesis of crystallized Bi_2WO_6. The whole process is displayed in Figure 5. In the beginning, the formation of tiny crystalline nuclei in a supersaturated medium occurred. Then the crystal growth followed. The larger particles grew at the cost of the small ones, due to the energy difference in solubility between the large particles and the smaller particles, according to the well-known Gibbs−Thomson law.[37] In early stages, an examination of the intermediate samples showed the coexistence of small laminar structure and irregular crystalline nuclei. As the reaction continued, irregular nanoparticles vanished and larger nanoplates formed.

(36) Yu, S. H.; Liu, B.; Mo, M. S.; Huang, J. H.; Liu, X. M.; Qian, Y. T. *Adv. Funct. Mater.* **2003**, *13*, 639.
(37) Mullin, J. W.; *Crystallization*, 3rd ed.; Butterworth-Heinemann: Oxford, U.K., 1997.

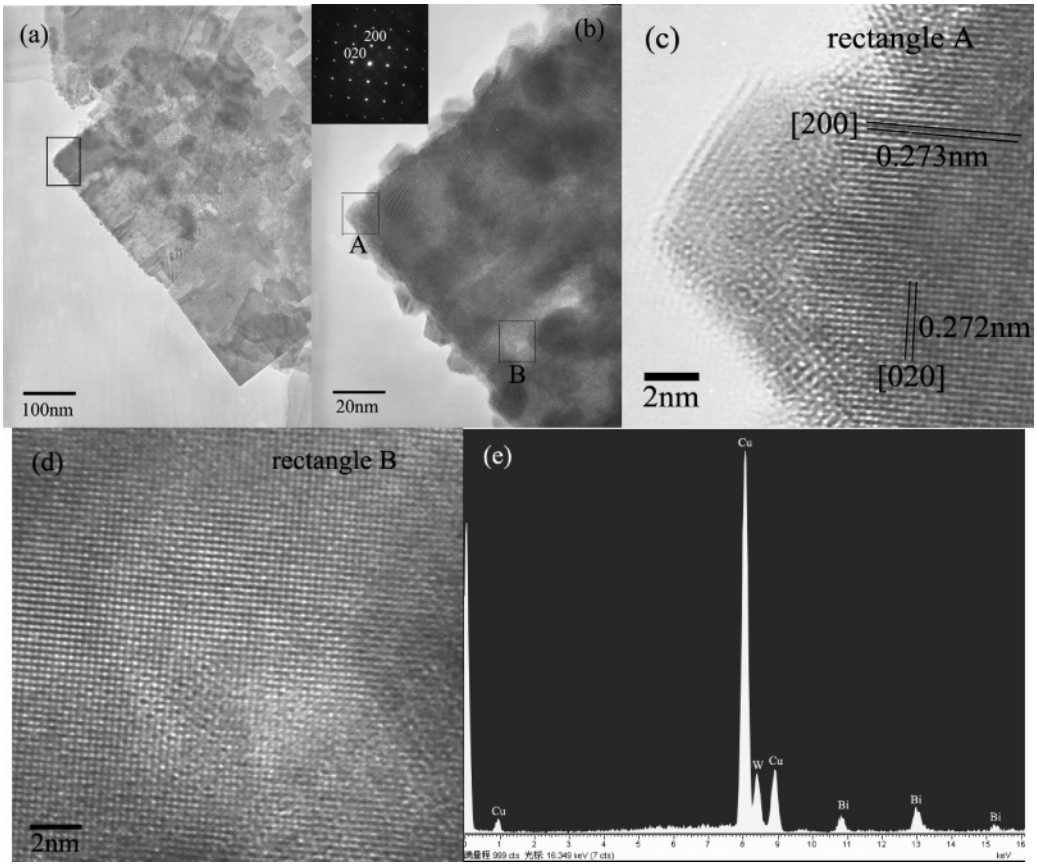

Figure 4. High-resolution transmission electron microscopy (HRTEM) images and EDAX spectrum of the Bi_2WO_6 nanoplates: (a) full view of the nanoplates (prepared at 200 °C, 12 h); (b) magnification of the rectangle in a and ED pattern; (c) HRTEM images of rectangle A in b; (d) HRTEM images of rectangle B in b; (e) EDAX spectrum of the Bi_2WO_6 nanoplates.

Table 1. Size, BET Surface Area, and Adsorption Percentage of Temperature Series Samples

sample	SSR sample	120 °C	140 °C	160 °C	180 °C	200 °C	220 °C	240 °C
av edge length (nm)	/	/	~50	~50	~100	~200	~200	/
BET surf areas (m^2/g)	1.24	32.58	24.64	22.85	20.97	21.34	19.63	17.08
adsorpn % in dark (%)	2.89	10.25	8.27	7.05	6.28	6.56	6.21	5.91

Table 2. Size, BET Surface Area, and Adsorption Percentage of Time Series Samples

sample	2 h	4 h	8 h	12 h	16 h	20 h	24 h	36 h
av edge length (nm)	/	~20	~40	~50	~60	~100	~100	~80
BET surf areas (m^2/g)	28.26	26.49	22.73	22.85	21.61	21.08	18.92	22.01
adsorpn % in dark (%)	11.62	8.54	7.60	7.05	7.29	6.92	6.43	7.24

This suggested that the larger nanoplates grew at the cost of the smaller particles. Tang had given schematic structure of the Bi_2WO_6 crystalline with orthorhomibic structures which are constructed by a corner-shared WO_6 octahedral layer and $Bi_2O_2^{2+}$ atom layers sandwiched between WO_6 octahedral layers.[31] On the basis of this structure which is shown in Figure 5, the layer was parallel to the (001) facets. In our hydrothermal condition, the precursor was prepared in neutral solution and washed several time to get rid of the other ions. So there were equal quantities of $Bi_2O_2^{2+}$ and WO_4^{2-} ions which were limited by K_{sp} of Bi_2WO_6 in the crystal growth process. Peng and Peng have shown that the shape of the nanostructures is strongly dependent on the relative chemical potential.[38] According to the Gibbs−Thompson theory, the relative chemical potential of crystals is simply proportional to their surface−atom ratio, which is determined by the average of dangling bonds per atom over the entire crystal.

The chains of octahedral-W usually play an important role in the high intrinsic anisotropic growth in various tungstates because of the facets which are perpendicular to these chains composed of highly distorted octahedral tungsten with dangling bonds. These facets usually have high chemical potential.[36] It is believed that two-dimensional growth occurs only if the chemical potential of two surfaces is much higher than others. Through the structure feature in Figure 4, the chains of octahedral-W equally existed along the *a*- and *b*-axes, which indicates the (200) and (020) facets had much higher chemical potential compared to other facets. This structure feature will make the (200) and (020) faces very sensitive to the surrounding growth conditions. This intrinsic anisotropic growth habit could happen when enough foreign energy (120 °C in our system) input overcomes the reaction barrier. The growth rates of the (200) and (020) faces are much higher. Further stochastic growth on the edge under electron beam exposure also confirmed that the nanoplates preferentially grow along the layer, which is shown in Figure 4b. According to the basic knowledge of crystallography, the faster crystal facets grow the more easily these facets disappear. Finally the morphologies of the samples are platelike with the edges of (220), ($2\bar{2}0$), ($\bar{2}20$), and ($\bar{2}20$) facets, which was confirmed by HRTEM results.

3.4. Band Gap of the Bi_2WO_6 Nanoplates. Optical absorption of the Bi_2WO_6 nanoplates was measured by using

(38) Peng, Z. A.; Peng, X. G. *J. Am. Chem. Soc.* **2002**, *124*, 3343.

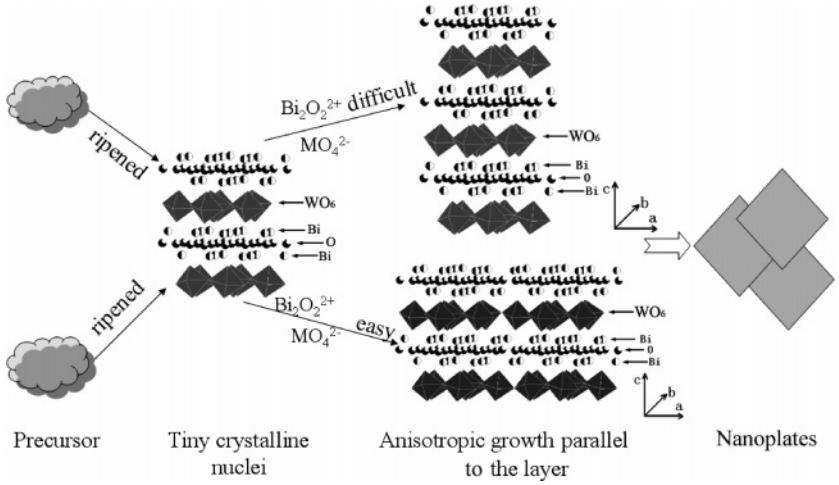

Figure 5. Growth mechanism of the nanoplates.

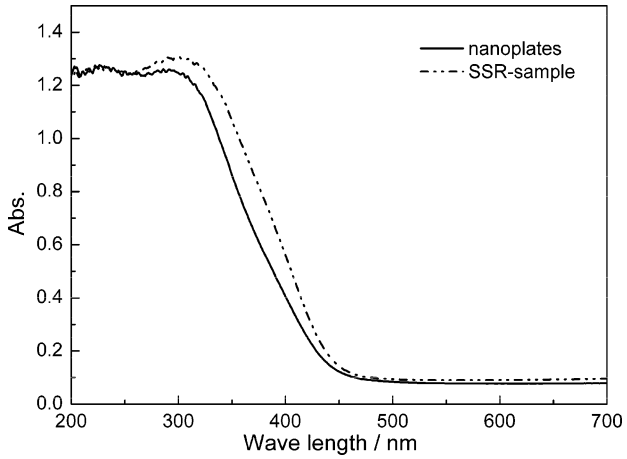

Figure 6. UV−vis spectra of Bi_2WO_6 nanoplates and SSR sample (Bi_2WO_6 prepared at 160 °C for 20 h).

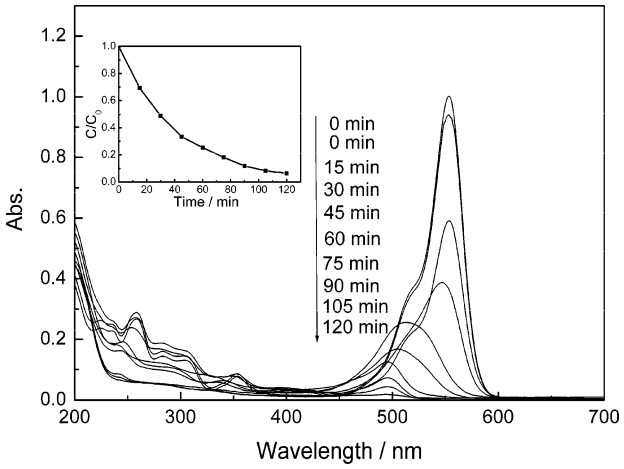

Figure 7. Absorption changes of RhB solution under photocatalytic process (0.1 g Bi_2WO_6 prepared at 160 °C for 12 h added into 200 mL of 10^{-5} mol/L RhB solution).

an UV−vis spectrometer. All optical absorption of the nanoplates was nearly the same. Figure 6 showed a typical diffuse reflection spectrum of good-quality Bi_2WO_6 nanoplates (160 °C, 20 h) compared to the solid-state reaction (SSR) sample. The solid-style curve represented Bi_2WO_6 nanoplates, and the dashed−dottted style curve represented the SSR sample. The steep shape of the spectra indicated that the visible light absorption was not due to the transition from the impurity level but was due to the band-gap transition.[39] For a crystalline semiconductor, it was shown that the optical absorption near the band edge follows the equation[40] $ah\upsilon = A(h\upsilon - E_g)^{n/2}$, where a, υ, E_g, and A are absorption coefficient, light frequency, band gap, and a constant, respectively. Among them, n decides the characteristics of the transition in a semiconductor. According to the equation, the value of n for Bi_2WO_6 was 1. The Bi ions charge in Bi_2WO_6 is +3. There are two 6s valence electrons of Bi in the crystalline phase. The band structure of Bi_2WO_6 was suggested to be composed of W_{5d} (conduction band, CB) and hybridization of Bi_{6s} and O_{2p} (valence band, VB). Compared to the SSR sample, the absorption of Bi_2WO_6 nanoplates appeared to blue-shift obviously. The band gap of the nanoplates was estimated to be 2.75 eV from the onset of the absorption edge, which was bigger than Zou's result (2.69 eV). This can be attributed to the nanosized effect. The color of the nanoplates was light yellow, as can be expected from the absorption spectrum.

3.5. Photocatalytic Activities. Temporal evolution of the spectral changes taking place during the photodegradation of RhB mediated by typical Bi_2WO_6 nanoplates (160 °C, 12 h) under visiable light is displayed in Figure 7.

Tetraethylated rhodamine, RhB, showed a major absorption band at 553 nm. In the presence of Bi_2WO_6 nanoplates, the absorbance decreases by ca. 7.05%, reflecting the extent of adsorption of RhB on Bi_2WO_6 nanoplates in the dark. Table 1 and Table 2 also show the BET surface areas and extent of the adsorption rate of the temperature and time series samples, respectively. Both in Table 1 and Table 2, it clearly revealed that either nanoparticles or nanoplates had much larger BET surface areas and can more efficiency adsorb RhB molecules than the SSR sample. The BET surface areas and extent adsorption rate decreased a little when the temperature was increased. But for time series samples, the same clination happened only before 24 h. Further long reaction time leads to diminution of the crystalline phase. The average length of the edge reduced to 80 nm so that the surface area and adsorption rate increased

(39) Kudo, A.; Tsuji, I.; Kato, H. *Chem. Commun.* **2002**, 1958.
(40) Butler, M. A. *Appl. Phys.* **1977**, *48*, 1914.

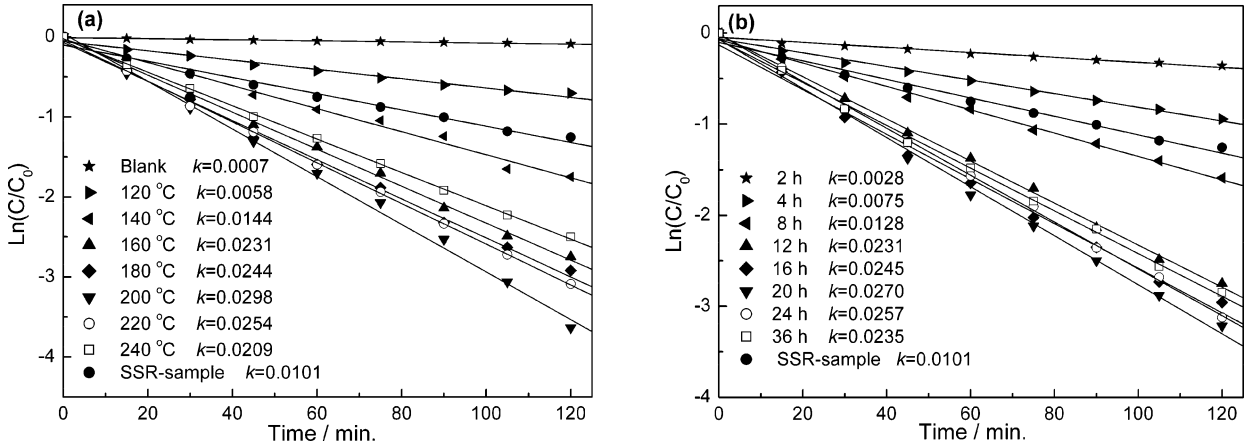

Figure 8. First-order plots for the photocatalytic degradation of RhB using various Bi_2WO_6 samples: (a) temperature series samples; (b) time series samples.

a little. Visible light irradiation of the aqueous RhB/Bi_2WO_6 nanoplate dispersion led to an apparent decrease in absorption.

In the photodegradation process, the major absorption band shifted to 500 nm step by step, reminiscent of similar hypsochromic shifts seen by Zhao et al. in the RhB/TiO_2 system.[41] Under visible illumination, the dye was de-ethylated in a stepwise manner with the color of the dispersion changing from initial red to a light green-yellow. De-ethylation of the fully *N*,*N*,*N*′,*N*′-tetraethylated rhodamine molecule (i.e., RhB) has the wavelength position of its major absorption band moved toward the blue region, λ_{max}, RhB, 552 nm; *N*,*N*,*N*′-triethylated rhodamine, 539 nm; *N*,*N*′-diethylated rhodamine, 522 nm; *N*-ethylated rhodamine, 510 nm; and rhodamine, 498 nm.[42] RhB formed rhodamine after being fully demethylated, and the rest was degraded through destruction of the conjugated structure. Figure 8a shows the degradation of rhodamine-B using temperature series Bi_2WO_6 samples. Total concentrations of all rhodamine species were simply determined by the maximum absorption measurement because the molar extinction coefficient ϵ_{max} of different rhodamine species were in a narrow range.[42] The first-order linear relationship was revealed by the plots of the $\ln(C/C_0)$ vs irradiation time (t). In this system, it can be explained in a Langmuir−Hinshelwood model. When solution was dilute, the reaction rate can be expressed by

$$r = kKC$$

K refers to adsorption equilibrium constant, *k* is reaction constant, and *C* is the concentration of the reactant. We could notice that RhB could degrade naturally, but the degradation rate was extremely slow. Among temperature series samples, only the sample prepared at 120 °C showed lower activities than the SSR sample. That sample is not high crystallinity, which is confirmed by the XRD result and TEM image. A lot of defects could act as an electron−hole recombination center. So the photocatalytic activity was low. Before 200 °C, the higher the treatment temperature is, the higher the activities performed. But above 160 °C, the temperature effect is not remarkable. The activity increased only a little, and the highest activity was obtained at 200 °C. When the temperature further increased, the activities decreased. It is mainly attributed to a worse crystalline phase and is consistent with the XRD and TEM results. Via the first-order linear fit, the determined reaction rate constant *k* was 0.0058, 0.0144, 0.0231, 0.0244, 0.0298, 0.0254, and 0.0209 min^{-1}, respectively, for the temperature series samples. In contrast, the constant *k* of the SSR sample was only 0.0101 min^{-1}.

When the temperature was settled at 160 °C, activities of the as-prepared sample could exceed that of the SSR sample after 8 h hydrothermal treatment. Figure 8b also shows the first-order plots for the photocatalytic degradation of RhB using time series Bi_2WO_6 samples. The reaction rate constant *k* was 0.0028, 0.0075, 0.0121, 0.0190, 0.0245, 0.027, 0.0257, and 0.0235 min^{-1}, respectively, for the 2, 4, 8, 12, 16, 20, 24, and 36 h samples. Good-quality nanoplates fabricated along with the reaction time and the activities increased corresponding to better crystallinity of the sample at the beginning. However, this inclination stopped at 20 h and further long hydrothermal treatment brought a decrease because of diminution of the nanoplates. Considering the nuance of the BET surface area between series samples, activities are more related to their morphology and crystallinity.

In sum, both temperature and time series comparison revealed that the Bi_2WO_6 nanoplates had special advantage in photocatalytic reaction. The most imaginable reason is that the Bi_2WO_6 nanoplates not only had large surface area to increase the reaction place but also promote the efficiency of the electron−hole separation. After all, the laminar structure is only several nanometers thick. Plenty of holes generated inside the crystalline had opportunity to transfer to the surface and act with the organic molecules.

4. Conclusions

Bi_2WO_6 nanoplates with square laminar morphologies have been successfully synthesized by hydrothermal treatment. The square nanoplates can be attributed to anisotropic growth in the crystalline-ripened process. The Bi_2WO_6 nanoplates could be formed at no less than 120 °C. The

(41) (a)Wu, T.; Liu, G.; Zhao, J. *J. Phys. Chem. B* **1998**, *102*, 5845. (b) Zhao, W.; Chen, C.; Li, X.; Zhao, J. *J. Phys. Chem. B* **2002**, *106*, 5022.

(42) (a) Watanabe, T.; Takizawa, T.; Honda, K. *J. Phys. Chem.* **1977**, *81*, 1845. (b) Inoue, T.; Watanabe, T.; Fujishima, A.; Honda, K.; Kohayakawa, K. *J. Electrochem. Soc.* **1977**, *124*, 719.

investigation of temperature and reaction time effects on nanoplates revealed good-quality nanoplates could be fabricated at 200 °C, 12 h or 160 °C, 20 h hydrothermal condition. The Bi_2WO_6 nanoplates performed high photocatalytic activities under visible light irradiation. The reaction constant can be three times that of the solid-state reaction sample in comparison experiments of RhB degradation.

Acknowledgment. This work was partly supported by the Chinese National Science Foundation (Grant 20433010), the Trans-Century Training Program Foundation for the Talents by the Ministry of Education, PRC, and supported by the Excellent Young Teacher Program of MOE, PRC.

CM0501517